Supplementary Information

First-principles study of ferroelectric and optical properties in (Zn, Co)-doped barium titanate

Xuebing Du[a], *Zheng Kang*[a], *Mei Wu*[a],*Dan Lin*[a], *Ancheng Wang*[b], *Yunkai Wu*[*a], *Xu Wang*[*c]

a: College of Big Data and Information Engineering, Guizhou University, Guiyang, 550025, Guizhou, China

b: Department of Mathematics, The Chinese University of Hong Kong, Hong Kong SAR 999077, China

c: Key Laboratory of Advanced Manufacturing Technology, Ministry of Education, Guiyang, 550025, Guizhou, China

*Corresponding author. E-mail: ykwu@gzu.edu.cn

**Corresponding author. E-mail: xuwang@gzu.edu.cn

Table S1. Formation energy (E_f) values of each system BZCT(Co^{2+}), BZCT(Co^{3+}) and BZCT(Co^{4+})

	BZCT(Co^{2+})	BZCT(Co^{3+})	BZCT(Co^{4+})
E_f(eV)	50.5561	96.1053	-4.4917

Table S2. BTO for different supercell sizes.

Supercell size	a=b	c	c/a	Band_Gap(eV)	P_s (μC/cm^2)
1×1×1	3.976	4.048	1.018	1.76	30
2×2×2	3.996	4.217	1.055	1.81	29.57
2×2×2(GGA+U)	3.991	4.041	1.013	3.2	26.86
3×3×3	3.967	4.067	1.025	1.76	——

The computational results demonstrate that parameters such as polarisation, bandgap, and lattice constant are consistent with experimental data and literature reports. This confirms that the influence of long-range interactions has been adequately accounted for within the computational framework employed in this study, and does not significantly compromise the core conclusions.

Table S3. Hubbard U parameter values are chosen for the O-2p, Ti-3d and Ba-5d orbitals of BTO cell, yielding gap energy values in good agreement with the experimental data, by using the GGA-PBE approximation.

U_d(Ba)	U_d(Ti)	U_p(O)	Eg(eV)
0	1	0	1.8029
0	2	0	1.9294
0	3	0	2.1770
0	4	0	2.1962

0	6	0	2.4816
0	7	0	2.6303
0	8	0	2.8885
0	9	0	3.0437
0	10	0	3.2018

Table S4. Convergence tests on cutoff energies in the range of 400-600 eV.

ENCUT(eV)	400	450	500	550	600
TOTEN(eV)	-320.5357	-320.3563	-320.3463	-320.3581	-320.4026
△ E(eV)	——	0.1793	0.0099	-0.0117	-0.04448

We calculated the energy deviations at other cutoff energies relative to the total energy at 500 eV. For instance, at a cutoff energy of 450 eV, the energy deviation was merely 0.0099 eV; whilst at 550 eV, the deviation was -0.0117 eV. Both deviations are substantially below the conventional convergence criterion of 0.05 eV/atom, falling within negligible error margins. This demonstrates that 500 eV adequately satisfies the truncation requirements for electron wave functions in the system, eliminating the need for higher truncation energies to achieve greater precision.

Table S5. K-point grid convergence tests.

KPOINTS	4×4×4	5×5×5	6×6×6	7×7×7
TOTEN(eV)	-320.3061	-320.3463	-320.3463	-320.3464

Increasing the K-point grid from 4×4×4 to 5×5×5 resulted in a significant decrease in total energy, which then stabilised. However, increasing it further, to 6×6×6 and 7×7×7, yielded negligible changes in total energy, falling within an insignificant range. This suggests that the 5×5×5 grid already meets the requirements for energy convergence. Enlarging the K-point grid further would substantially increase computational costs without significantly improving computational accuracy. Consequently, the 5×5×5 K-point grid was selected for subsequent structural optimisation and electronic structure calculations.

Table S6. Comparison of GGA+U with Hybrid Functional (HSE06).

	GGA+U	HSE06
E_g(eV)	3.20	3.22

The band gap calculated using GGA+U is 3.20 eV, while the HSE06 calculation yields 3.22 eV, representing a deviation of merely 0.6%. The GGA+U method employed in this study adequately describes the influence of long-range Coulomb interactions on electronic structure (band gap). Furthermore, owing to practical computational constraints, the band gap and lattice constant values obtained via GGA+U calculations are already highly consistent with experimental data. Consequently, these results provide a reliable foundation for subsequent investigations, eliminating the need for more computationally intensive hybrid functionals in follow-up calculations.

Table S7. Table of energies of individual atoms($\boldsymbol{\mu}_{\mathrm{Zn}}$, $\boldsymbol{\mu}_{\mathrm{Co}}$, $\boldsymbol{\mu}_{\mathrm{Ba}}$, $\boldsymbol{\mu}_{\mathrm{Ti}}$) and substitution energy ($\boldsymbol{E}_{\mathrm{f}}$) data for systems with different doping sites of the elements. The four identifiers, Zn(Ba), Zn(Ti), Co(Ba) and Co(Ti) are preceded by the individual elements doped, and inside the parentheses are the substituted atomic sites.

Energy/ eV	Zn(Ba)	Zn(Ti)	Co(Ba)	Co(Ti)
E_{doped}	-330.33274827	-321.24961857	-331.81496668	-327.39082757
μ_{Zn}	-10.54035702			
μ_{Co}			-11.35391924	
μ_{Ba}	-3.93582114			
μ_{Ti}	-8.94622768			
E_{pure}	-320.17490499			
E_{f}	-3.5533074	0.74153405	-4.22196359	-4.8082310

As demonstrated in the table, Zn exhibits a lower formation energy at Ba sites and Co at Ti sites. This suggests that the stability of the substituent site is enhanced, as indicated by the lower substitution energy. Consequently, the substitution of Zn^{2+} at Ba^{2+} sites and Co^{2+} at Ti^{4+} sites is more feasible.

Table S8. Formation energy (E_f) values and the energy of each system(E_{doped}, E_{pure}) and elements (μ_{Zn}， μ_{Co}， μ_{Ba}， μ_{Ti}) .

	Energy(eV)
E_{pure}	-320.39445262
$E_{\text{doped}}(Co^{2+})$	-266.38204588
$E_{\text{doped}}(Co^{3+})$	-541.22724457
$E_{\text{doped}}(Co^{4+})$	-321.42991954
μ_{Zn}	-1.11247205
μ_{Co}	-6.81992599

μ_{Ba}	-3.5469440725
μ_{Ti}	-7.8417359767

Figure S1. Models of different Co ion valence states: (a) BZCT (Co^{2+}) and (b) BZCT (Co^{3+})

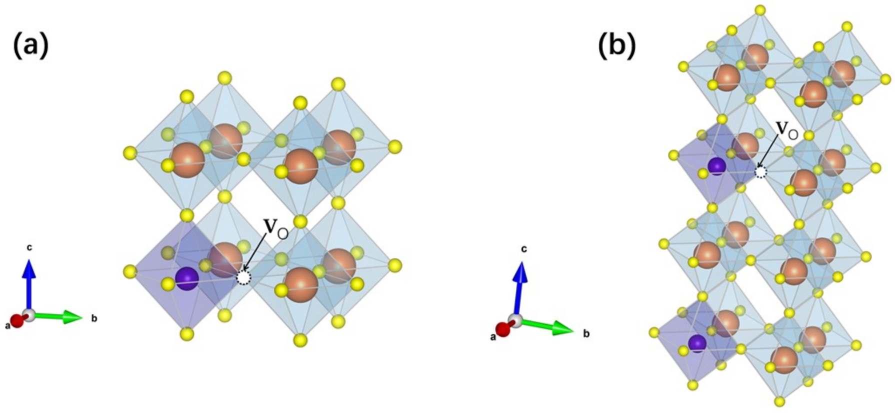

When Ti^{4+} at site B is replaced by lower-valent Co^{2+} or Co^{3+}, the system experiences charge imbalance due to the loss of positive charge. The formation of oxygen vacancies restores lattice charge neutrality by reducing negative charge (loss of O^{2-}) — this represents the most typical charge compensation mechanism in cobalt-doped BTO systems. In the 2×2×2 supercell depicted in Figure S1(a), the single oxygen vacancy introduced by Co^{2+} doping forms a local charge-balanced unit with the dopant ion. Conversely, in the 2×2×4 supercell shown in Figure S1(b), the oxygen vacancies corresponding to Co^{3+} doping are distributed across a larger-scale lattice.

Figure S2. Band structures and density of states for different Co ion valence states:(a) Band structure of BZCT (Co^{2+}), (b) Band structure of BZCT (Co^{3+}), (c) DOS of BZCT (Co^{2+}), (d) DOS of BZCT (Co^{3+})

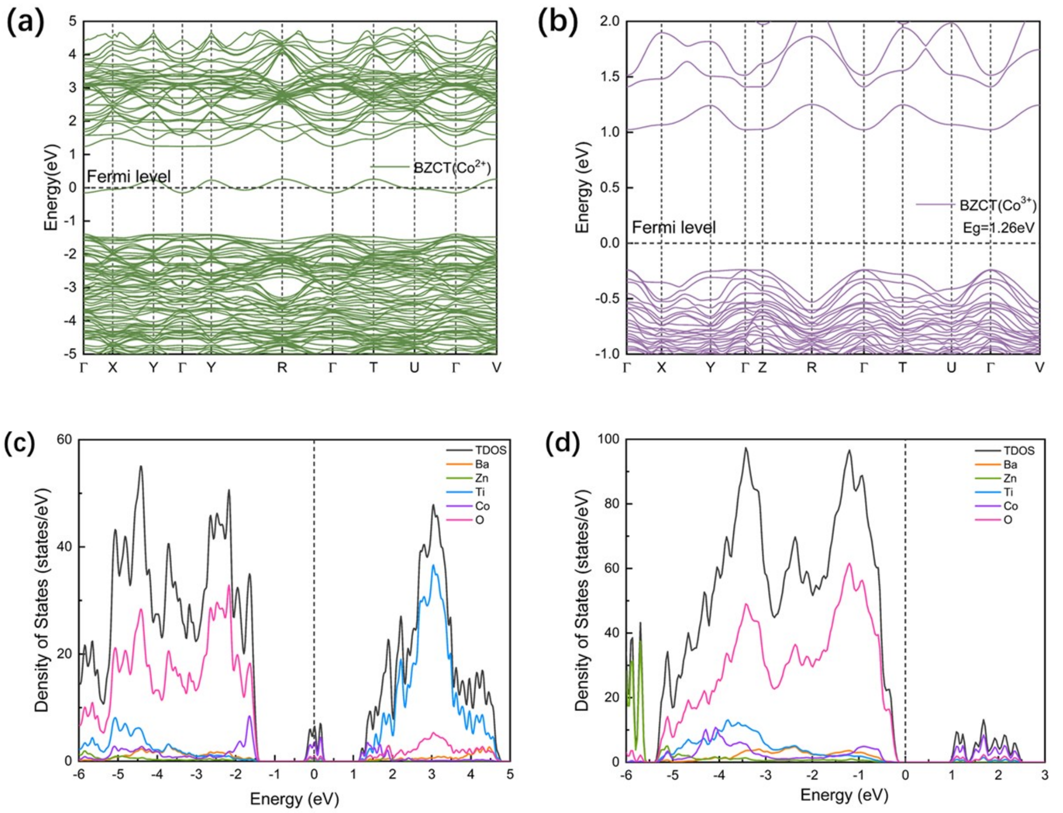

Combining the band structure in Figure S2(a) with the density of states in Figure S2(c), we observe a distinct impurity level at the Fermi level. However, the absence of a significant band gap precludes further computational analysis. This suggests that BZCT (Co^{2+}) exhibits metallic band characteristics, which correspond to the hybridisation of Co-O orbitals at the Fermi level in the density of states. Figure S2(b) shows that the Fermi level resides within the band gap; however, the extremely narrow gap (Eg = 1.26 eV) exhibits the characteristics typical of a narrow-bandgap semiconductor. Although no band overlap is evident at the Fermi level, the band gap is considerably smaller than that of BZCT(Co^{4+}, Eg = 2.34 eV). Figure S2(d) shows that the total density of states near the Fermi level (at 0 eV) approaches zero, while the valence band top (-1~ 0 eV) is dominated by O 2p and Co 3d orbitals.

Figure S3. Bond length and bond angle diagrams for (a) BTO and (b) BZCT octahedra

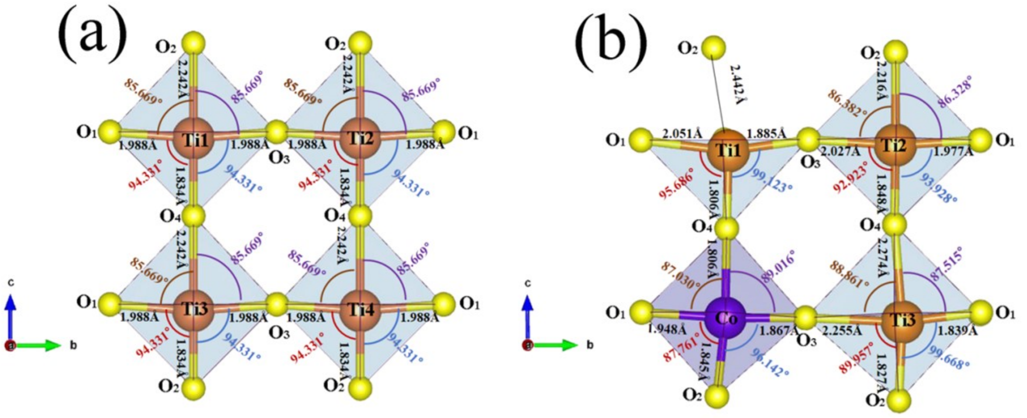

Figure S4. The band structures and band gaps of (a) BZTO and (b) BTCO.

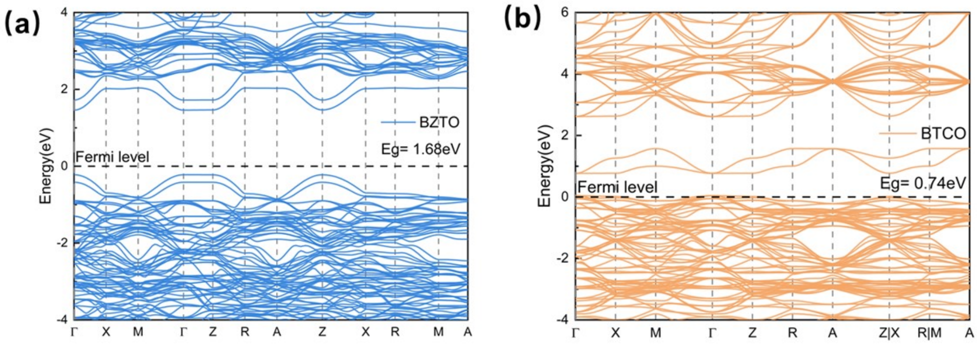

Figure S5. Electrical conductivity of BTO, BZTO, BTCOand BZCT

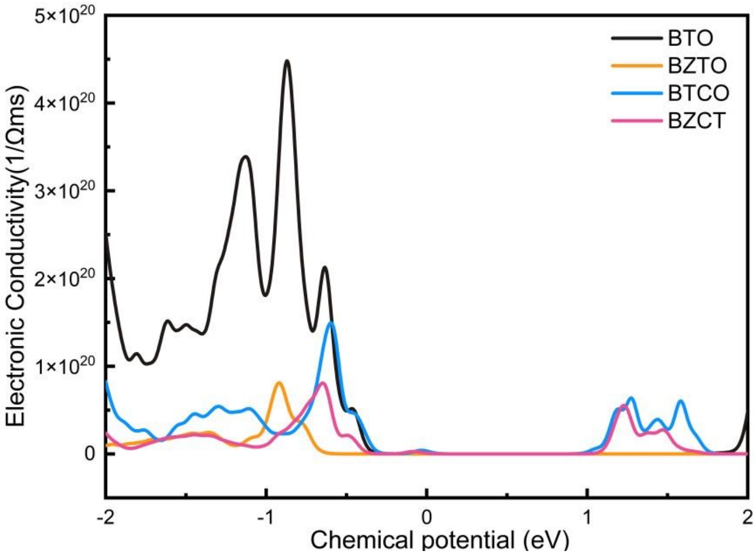

These calculations were grounded in the semi-empirical framework of the Boltzmann transport theory. The conductivity σ can be obtained by integrating the distribution function(equation 1) over the whole space[47]:

$$\sigma_{\alpha\beta}(T;\mu)=\frac{1}{\Omega}\int\sigma_{\alpha\beta}(\varepsilon)[\frac{\partial f_{\mu}(T;\varepsilon)}{\partial\varepsilon}]$$

where $f_{\mu}(T,\varepsilon)$ is the Fermi-Dirac distribution function, μ is the chemical potential and T is the temperature. When a constant relaxation time is known, it can be shown that the conductivity at RTA and RBA can be obtained for a certain chemical potential and temperature by calculating the energy band structure.A comparative analysis of the conductivity and relaxation time between the individual systems is illustrated in Figure S3, where the horizontal coordinates are the maximum and minimum values of the chemical potential with respect to the Fermi energy level.